The Astrophysical Journal, 1003:50 (15pp), 2026 May 20 https://doi.org/10.3847/1538-4357/ae5c98

Morphological Complexity of NGC 628—A Multiwavelength Multiscale Analysis Using the Ordinal Pattern Framework

Athokpam Langlen Chanu[1,2], S. Amrutha[3,4], Pravabati Chingangbam[3,4], and Changbom Park[5]
[1] Asia Pacific Center for Theoretical Physics, Pohang, 37673, Republic of Korea
[2] Department of Physics, Pohang University of Science and Technology (POSTECH), Pohang, 37673, Republic of Korea
[3] Indian Institute of Astrophysics, Koramangala II Block, Bangalore 560034, India; prava@iiap.res.in
[4] Pondicherry University, R.V. Nagar, Kalapet, 605014, Puducherry, India
[5] School of Physics, Korea Institute for Advanced Study, 85 Hoegiro, Dongdaemun-gu, Seoul, 02455, Republic of Korea
Received 2025 September 6; revised 2026 April 4; accepted 2026 April 6; published 2026 May 13

Abstract

As statistical systems, galaxies exhibit a rich interplay between organized structure and stochastic fluctuations across a broad range of spatial scales. This duality motivates the need for quantitative frameworks capable of capturing their morphological complexity. The ordinal patterns framework, along with its associated statistical measures: permutation entropy (H), disequilibrium (D_E), statistical complexity (C), and ordinal network node entropy, has recently emerged as a powerful tool for analyzing such complexity in physical systems. We apply this framework in a multiwavelength, multiscale analysis of the galaxy NGC 628, utilizing observations in the near-ultraviolet, near-infrared, mid-infrared, and millimeter bands. Our results reveal a characteristic spatial scale of approximately 200 pc, marking the transition from small-scale structures influenced by star formation and stellar feedback to larger-scale morphology governed by the galaxy's dynamics. Furthermore, we find that the C versus H trajectories for all wavelengths converge toward a common attractor curve, consistent with the behavior of isotropic Gaussian random fields. This convergence suggests a universal statistical behavior in galactic structure at large scales, despite the differing physical processes traced by each wavelength.

Unified Astronomy Thesaurus concepts: Galaxies (573)

1. Introduction

Complexity of statistical systems is a multifaceted concept, with numerous complexity measures proposed across disciplines (S. Lloyd 2001; R. Friedrich et al. 2011; A. Roli et al. 2019). Traditional complexity measures include Lyapunov exponents (A. Wolf et al. 1985), fractal dimensions (B. B. Mandelbrot 1985), and entropy (T. M. Cover 1999), each offering a distinct perspective on the underlying characteristics of complex systems.

R. Lopez-Ruiz et al. (1995) introduced a statistical measure of complexity based on the distance of the probability distribution of "accessible states" of a given system from an equiprobable distribution, multiplied with the Shannon entropy (C. E. Shannon 1948). This complexity measure and Shannon entropy encode complementary information of order and disorder. The so-called *complexity-entropy plane* then serves as a phase space on which different physical systems take values, allowing for distinction by their degree of complexity. This characterization of physical systems depends on the "scale of observations" as the space of accessible states varies with observation scale.

C. Bandt & B. Pompe (2002) introduced the so-called *permutation entropy* (H), as an information-theoretic measure of the complexity of 1D empirical data, by constructing accessible states based on comparison of neighboring data values and symbolic dynamics (G. Balasis et al. 2013). O. A. Rosso et al. (2007) extended the formalism and proposed a statistical complexity measure (C) based on the notion of complexity introduced in R. Lopez-Ruiz et al. (1995), and used the complexity-entropy (CH) plane to distinguish different systems. H. V. Ribeiro et al. (2012) and L. Zunino & H. V. Ribeiro (2016) further extended the formalism to 2D data, which is used to investigate spatial structures (L. Zunino & H. V. Ribeiro 2016; H. Y. Sigaki et al. 2018, 2019; C. Morel & A. Humeau-Heurtier 2021) in image analysis. The formalism of CH-plane has been widely used to distinguish *complex structures* across different physical domains (X. Mao et al. 2019; A. L. Chanu et al. 2024, 2025; M. K. Singh et al. 2026). Further, one can construct the so-called *ordinal networks* from transitions among accessible states (A. A. Pessa & H. V. Ribeiro 2019) that can extract additional distinguishing features in different datasets (see, e.g., A. A. Pessa & H. V. Ribeiro 2020, 2021).

Astrophysical systems—ranging from sunspot cycles, turbulent plasmas, orbital systems to galaxy morphologies and large-scale structure—exhibit rich complexity shaped by nonlinear processes, feedback, and multiscale interactions (S. N. Shore & D. Galli 2003; O. Regev 2006; G. Consolini et al. 2009; M. Aschwanden 2011; F. Fiore et al. 2024; A. Langlen Chanu et al. 2024; S. Ó. Hyman et al. 2025). This paper is focused on the complexity of galaxy morphologies. Galaxies constitute an important dynamical component of our observable Universe. Various studies have shown that the morphology of galaxies correlates with their physical properties, including mass, specific star formation rate, gas fraction, and integrated colors (e.g., $(g - r)$, $(B - V)$), among others (J. R. Gott & T. X. Thuan 1976; B. M. Poggianti et al. 2009; M. Cano-Díaz et al. 2019). For instance, elliptical galaxies are generally more massive than spiral galaxies. Since elliptical galaxies have already consumed most of their gas to form stars, they exhibit low gas fractions and show no recent star formation, making them appear red compared to late-type spirals. Thus,

morphological classification is crucial for understanding galaxy formation, evolution, and the underlying physical processes.

Existing classification methods primarily rely on visually distinguishing morphological features (E. P. Hubble 1936; G. De Vaucouleurs 1959). More recent approaches use improved photometric and spectroscopic data (S. A. Kauffman et al. 1993; A. J. Connolly et al. 1995; C. W. Yip et al. 2004), and automated intelligent techniques, including machine learning, to classify large numbers of galaxies (C. Lintott et al. 2011; X.-P. Zhu et al. 2019; B. E. Robertson et al. 2023). There are other nonparametric techniques describing the shape and light distribution of galaxies that are commonly used to classify the galaxies (J. M. Lotz et al. 2004; A. W. Graham & S. P. Driver 2005; C. J. Conselice 2006).

The structural and dynamical features of galaxies make them ideal for analysis using tools from the statistical physics of complex systems. In this pilot study, we assess the use of ordinal patterns and associated measures—permutation entropy, statistical complexity, and ordinal network node entropy—for classifying galaxy morphology. We select NGC 628 (the Phantom Galaxy), a well-studied, face-on spiral galaxy with high-resolution, multiwavelength data, meeting criteria for 2D-analysis, emission diversity, and data accessibility. NGC 628 has been extensively studied across a broad spectrum of wavelengths, from radio frequencies to X-rays (see J. Kamphuis & F. Briggs 1992; R. Soria & A. K. H. Kong 2002; K. Kreckel et al. 2018; J. C. Lee et al. 2023). In this study, using near-ultraviolet (NUV), near-infrared (NIR), mid-infrared (MIR), and millimeter (mm) images, we quantify its morphological complexity across wavelengths.

The ordinal pattern framework and in particular the *CH*-plane has been previously used to study magnetic flux ropes in the corona of the Sun (W. Gekelman et al. 2019), turbulence in the solar wind (P. J. Weck et al. 2015; J. M. Weygand & M. G. Kivelson 2019), electron plasma pressure filaments (S. Karbashewski et al. 2022), characterization of exoplanet systems (G. J. Gilbert & D. C. Fabrycky 2020; S. Bartlett et al. 2022), and X-ray (M. Lovallo & L. Telesca 2011) and radio astrophysical sources (G. Segal et al. 2019). Applying information-theoretic metrics such as entropy and statistical complexity has yielded valuable insights across astrophysical systems. For example, S. Bartlett et al. (2022) demonstrated that these metrics effectively characterize planetary features and can assist in detecting potential biospheres in exoplanet studies. J. M. Weygand & M. G. Kivelson (2019) used them to reveal the stochastic behavior of solar wind structures, including interplanetary coronal mass ejections, corotating interaction regions, and turbulent magnetic fluctuation intervals. Likewise, G. Segal et al. (2019) showed their ability to distinguish simple and complex radio galaxy morphologies in data from the Australia Telescope Large Area Survey.

This paper is organized as follows. Section 2 outlines the framework of ordinal patterns, permutation entropy, statistical complexity, and ordinal networks, along with their physical interpretations. Section 3 describes the multiwavelength data and physics of NGC 628. In Section 4, we present our main analysis and results. Finally, Section 5 concludes with a summary and discusses the implications of our findings and future directions.

2. Framework of Ordinal Patterns, Permutation Entropy, Statistical Complexity, and Ordinal Networks

This section introduces the main concepts used in our analysis, namely, ordinal patterns, permutation entropy, statistical complexity, complexity-entropy causality plane, and ordinal networks. This section follows A. A. Pessa & H. V. Ribeiro (2021).

Consider an $N_x \times N_y$ data matrix Y whose elements are Y_i^j, with $i = 1, 2, \ldots, N_x, j = 1, 2, \ldots, N_y$. For a fixed (i, j), let y be a submatrix of size $d_x \times d_y$:

$$y = \begin{bmatrix} Y_i^j & Y_i^{j+1} & \cdots & Y_i^{j+(d_y-1)} \\ Y_{i+1}^j & Y_{i+1}^{j+1} & \cdots & Y_{i+1}^{j+(d_y-1)} \\ \vdots & \vdots & \ddots & \vdots \\ Y_{i+(d_x-1)}^j & Y_{i+(d_x-1)}^{j+1} & \cdots & Y_{i+(d_x-1)}^{j+(d_y-1)} \end{bmatrix}. \quad (1)$$

d_x, d_y are referred to as "embedding dimensions." The smallest choice is $d_x = 2 = d_y$, in which case y is a 2×2 matrix. Moreover, they are chosen to satisfy $d_x \ll N_x$, $d_y \ll N_y$ with $(d_x d_y)! \ll N_x N_y$. This condition is necessary to get a reliable estimate of the ordinal probability distribution, which will be defined shortly.

Let us denote $n_x \equiv N_x - (d_x - 1)$ and $n_y \equiv N_y - (d_y - 1)$. By varying i from 1 to n_x, and j from 1 to n_y in steps of one, we can construct $n_x n_y$ number of such y submatrices. In general, the steps for i and j can be arbitrary positive integers, usually known as *embedding delays*. Here we restrict to unit embedding delays.

Permutation state or ordinal pattern. Every submatrix y can be mapped to a "permutation state" or "ordinal pattern" by the following procedure.

1. *Flatten the elements of* y. Write the elements of y as a 1D sequence denoted by $z = \{z_1, z_2, \ldots, z_{d_x d_y}\}$ (referred to as the "flattening" step). There is no unique way to flatten y. We choose one way of doing it consistently for all y.
2. *Map* z *to a symbolic sequence* A. We assign an integer sequentially to each element of z as,

$$\{z_m\} \rightarrow \{(m-1)\} \equiv A, \qquad m = 1, 2, \ldots, d_x d_y. \quad (2)$$

   A is a symbolic sequence because its integer elements only serve as position markers or indices for the elements of z.
3. *Sorting and permutation*. Next, the elements of z are sorted in ascending order to get another sequence z_S, resulting in the elements of A getting shuffled or permuted to get another sequence A_S. The new sequence A_S is referred to as a "permutation state" or "ordinal pattern." Other terms such as "permutation pattern," "ordinal state," and "permutation symbol" are also used in the literature.

The steps 1–3 above map every submatrix y to a permutation state. We introduce the symbol π_i^j, $i = 1, 2, \ldots, n_x$, $j = 1, 3, \ldots, n_y$, to denote a permutation state. The sequence $\{\pi_i^j\}_{i=1,2,3,\ldots,n_x}^{j=1,2,3,\ldots,n_y}$ is referred to as the *ordinal sequence*. It is just the set of all $n_x n_y$ number of permutation states obtained from Y. An illustration of the computation of permutation states for an example 2D array is given in Appendix A.

Ordinal probability distribution. Given $d_x d_y$ number of distinct nonnegative integers, we have $(d_x d_y)!$ distinct states. Under the condition $N_x N_y \sim n_x n_y \gg (d_x d_y)!$, not all states in the ordinal sequence will be distinct. Let us denote each distinct state by ψ_k, where $k = 1, 2, \ldots, (d_x d_y)!$. Let n_k denote the number of occurrences of each ψ_k in the ordinal sequence. Then, the probability of occurrence of each ψ_k is given by:

$$\rho_k(\psi_k) = \frac{n_k(\psi_k)}{n_x n_y}. \tag{3}$$

The function $P = \{\rho_k(\psi_k)\}$ is referred to as the *ordinal probability distribution*. It satisfies the normalization condition:

$$\sum_{k=1}^{(d_x d_y)!} P = \sum_{k=1}^{(d_x d_y)!} \rho_k(\psi_k) = 1. \tag{4}$$

Having introduced the basic concepts of ordinal patterns, we now introduce the statistical quantities that we will use to analyze the galaxy data.

2.1. Permutation Entropy, Statistical Complexity, and the Complexity-entropy (CH) Causality Plane

Permutation entropy, $H[P]$. The functional $S[P]$ expressed by

$$S[P] = -\sum_{k=1}^{(d_x d_y)!} \rho_k(\psi_k) \log_2 \rho_k(\psi_k) \tag{5}$$

is the entropy of the permutation states (C. Bandt & B. Pompe 2002). Then the *normalized* permutation entropy, $H[P]$ (O. A. Rosso et al. 2007), is defined as

$$H = \frac{S[P]}{\log_2 (d_x d_y)!}, \tag{6}$$

where the normalization factor $\log_2 (d_x d_y)!$ is the maximum entropy; thus, H satisfies $0 \leqslant H \leqslant 1$. H (or S) provides a measure of the degree of disorder or randomness of the data Y, with $H \to 1$ indicating high disorder.

H is exactly 1 when Y consists of totally random elements and all distinct permutation states are equiprobable, whereas when physical correlations are present in the data across scales set by (d_x, d_y), some states have higher probabilities, hence $H < 1$. The higher the correlation strength, the lower the value of H.

Statistical complexity, $C[P, U]$. Let U denote the uniform probability distribution, $U = \{u_k\}$, with $k = 1, 2, \ldots, (d_x d_y)!$, where $u_k = 1/(d_x d_y)!$. The Jensen–Shannon divergence between the probability distributions P and U is given by

$$D[P, U] = S\left[\frac{(P + U)}{2}\right] - \frac{S[P]}{2} - \frac{S[U]}{2}, \tag{7}$$

with permutation entropy of P, $S[P]$ (Equation (5)), and permutation entropy of U, $S[U]$ given by

$$S[U] = -\sum_{k=1}^{(d_x d_y)!} u_k \log_2 u_k. \tag{8}$$

$P + U$ is the mixture distribution of P and U, and its corresponding permutation entropy is

$$S\left[\frac{P + U}{2}\right] = -\sum_{k=1}^{(d_x d_y)!} \left(\frac{\rho_k + u_k}{2}\right) \log_2 \left(\frac{\rho_k + u_k}{2}\right). \tag{9}$$

D of Equation (7) measures how different P is from U. It is nonzero when there exist more likely states in the space of states constructed from Y.

The so-called *disequilibrium* (M. Martin et al. 2003), denoted by D_E, is defined as the normalized Jensen–Shannon divergence,

$$D_E[P, U] = \frac{D[P, U]}{D_{\max}}, \tag{10}$$

where $D_{\max}$ denote the maximum possible value of $D[P, U]$ obtained when P is 1 and U vanishes as:

$$D_{\max} = -\frac{1}{2}\left\{\left[\frac{(d_x d_y)! + 1}{(d_x d_y)!}\right] \log[(d_x d_y)! + 1] - 2\log[2(d_x d_y)!] + \log(d_x d_y)!\right\}. \tag{11}$$

D_E (or D) provides a measure of order and organization in the data Y since it measures how far the ordinal probability distribution of Y is from an equiprobable distribution (representing equilibrium). By definition, $0 \leqslant D_E \leqslant 1$. Finally, the *statistical complexity*, C (O. A. Rosso et al. 2007) is defined to be:

$$C = D_E[P, U] \quad H[P]. \tag{12}$$

Complexity-entropy (*CH*) *plane*. For a given data Y, and for chosen (d_x, d_y) values, the computed values of H and C occupy a point (H, C) on the *CH*-plane with H on the x-axis and C on the y-axis. Datasets of different physical origins, for example, stochastic processes such as white noise, colored noise, and fractional Brownian motion or chaotic processes such as Lorenz, logistic map will typically occupy distinct regions of the *CH*-plane and hence can be distinguished (O. A. Rosso et al. 2007).

The entropy and complexity measures defined above have various attractive properties (C. Bandt & B. Pompe 2002; O. A. Rosso et al. 2007). The permutation patterns naturally emerge from the data without the need for any parameterization. Moreover, the results are unaffected by the presence of low levels of noise, invariant under monotonic transformations of the data values, and are also computationally inexpensive.

It is useful to analyze a given 2D-data using different choices of (d_x, d_y) because they probe spatial correlations at varying scales. For a given (N_x, N_y), as we increase d_x and d_y, the total number of permutation states given by $n_x n_y$ decreases, while the number of distinct states $(d_x, d_y)!$ grows factorially. This leads to a decrease of H due to the normalization factor in Equation (6), unless the data contains unusual scale dependence. In comparison, the behavior of C is not straightforward to anticipate. Further, interchanging d_x and d_y is equivalent to rotating the data by 90°, which can yield different H and C if the system lacks rotational symmetry, making such analysis useful for probing anisotropy.

2.2. Node Entropies from Ordinal Network

The ordinal patterns from the data matrix Y can be mapped into the nodes of an ordinal network (M. Small et al. 2018; A. A. Pessa & H. V. Ribeiro 2019). Each basis state ψ_k corresponds to a node, yielding $k = 1, 2, \ldots, (d_x d_y)!$ nodes. Directed edges connect adjacent basis states (horizontal or vertical), representing *transition* between the states. Suppose $n_{k\to m}$ denotes the total number of occurrences of a transition $\psi_k \to \psi_m$. Then the *weighted adjacency matrix* is:

$$\rho_{k,m} = \frac{n_{k\to m}}{2n_x n_y - n_x - n_y}. \tag{13}$$

The denominator represents the total number of horizontal and vertical transitions. Then the normalized transition probability is:

$$\rho'_{k,m} = \frac{\rho_{k,m}}{\sum_{m\in\mathcal{O}_k}\rho_{k,m}}, \tag{14}$$

where $\mathcal{O}_k$ is the set of all outgoing edges from node k.

We focus on the entropy measures that take into account the probabilistic nature of nodes and edges *locally*, and *globally* for the ordinal network. The *local node entropy* (M. McCullough et al. 2017; M. Small et al. 2018; A. A. Pessa & H. V. Ribeiro 2020)

$$s_k = -\sum_{m\in\mathcal{O}_k} \rho'_{k,m}\log\rho'_{k,m}, \tag{15}$$

measures determinism in the transitions at the node level (A. A. Pessa & H. V. Ribeiro 2020); $s_k = 0$ if only one edge exits k, and is maximum when all edges leaving k have the same weight (equiprobability).

The *global node entropy* (A. A. Pessa & H. V. Ribeiro 2020)

$$\mathrm{S_{gn}} = \sum_{k=1}^{(d_x d_y)!} \rho_k s_k, \tag{16}$$

is the weighted average of local entropies over all nodes of the network, with ρ_k being the probability of occurrence of each ψ_k (Equation (3)).

2.3. Ordinal Pattern Analysis for Gaussian Random Fields—A Toy Example

Before analyzing the morphological complexity of NGC 628, we first evaluate permutation entropy (H), statistical complexity (C), CH-plane, and global node entropy ($\mathrm{S_{gn}}$), as described in Sections 2.1 and 2.2, for realizations of Gaussian random fields (GRFs), which provide benchmarks for interpreting the galaxy's results.

We simulate GRFs with zero mean and unit variance on a 500 × 500 pixel grid, approximately comparable to the galaxy data. Uncorrelated, isotropic Gaussian white noise is generated in Fourier space, smoothed using a Gaussian kernel with standard deviation s (in pixel units), and then inverse-transformed. s introduces a characteristic smoothing scale. Hereafter, we refer to this as Gaussian smoothing. Larger s suppresses high-frequency (large k) modes, resulting in smoother, large-scale fluctuations. Conversely, a smaller s retains high-frequency components, producing finer, small-scale structures. We vary s to study how H, C, and $\mathrm{S_{gn}}$ change as functions of spatial scale.

Figure 1 shows realizations of the GRF for a fixed random seed with varying s (top row). We compute H and C for these GRFs, using embedding dimensions: $(d_x, d_y) = (2, 2)$, (2, 3), and (2, 4). For all (d_x, d_y) pairs, H decreases with increasing s. This can be visually inferred from the fact that for low s the GRFs contain more modes (hence more information and disorder), while for large s, the field becomes smoother and more ordered. For fixed s, H have lower values for higher (d_x, d_y), which is expected (see discussion in Section 2.1).

C exhibits a rapid increase at low s, reaches a maximum (seen for the higher (d_x, d_y) values in Figure 1), and then tends to decrease. The curves for different embedding dimensions cross each other due to different rates of increase and subsequent decrease with increasing s. For improved visual clarity, we show these H and C results in semi-log plots in the left and middle panels of the second row of Figure 1.

The right panel presents the CH-plane for the three embedding dimensions, with the black arrows indicating the direction of increasing s.

Limit of perfect correlation. In the above discussion, we focus on smoothing scales s that are in the ballpark range appropriate for the galaxy data in the next section. In the limit $s \to \infty$ (a completely uniform field), the field tends to a constant function, and $H \to 0$, $C \to 0$.

We now map the GRFs at each s to ordinal networks and calculate the horizontal and vertical global node entropies, $\mathrm{S_{gn}^{hor}}$ and $\mathrm{S_{gn}^{ver}}$, respectively. In the bottom row of Figure 1, we plot the variation of $\mathrm{S_{gn}^{hor}}$ (dotted), and $\mathrm{S_{gn}^{ver}}$ (dashed) with s (left), along with their difference, $\Delta\mathrm{S_{gn}}$ (middle). $\Delta\mathrm{S_{gn}}$ decreases with s and approaches zero, capturing directional asymmetries at small scales. Next, in the right panel, we fit an inverse power-law function (solid green line) to $\Delta\mathrm{S_{gn}}(s)$ (green triangles) in a log–log plot, yielding $\Delta\mathrm{S_{gn}}(s) = 18.58 \times s^{-1.18}$ with a goodness-of-fit value of $R^2 = 0.166$, indicating not particularly good fit. Investigating similar relations in the NGC 628 data may reveal signatures of self-organization arising from multi-scale physical interactions in the galaxy.

3. NGC 628 Galaxy—Multiwavelength View and Observed Data

The galaxy NGC 628 is a nearly face-on ($i = 8.^{\circ}9$; P. Lang et al. 2020) grand design spiral galaxy (SA(s)C; G. de Vaucouleurs et al. 1991) at a distance of 9.84 Mpc (G. S. Anand et al. 2020). It is a massive galaxy ($\log(M_*/M_\odot) = 10.34$; A. K. Leroy et al. 2019) with extended neutral hydrogen and UV disk (J. Kamphuis & F. Briggs 1992; D. A. Thilker et al. 2007; J. Yadav et al. 2021).

In this section, we describe the multiwavelength imaging data used in our study and also overview physical features observed across the wavelengths of NUV, NIR, MIR, and mm, as shown in Figure 2(a).

3.1. Multiwavelength Observed Data of NGC 628

We use archival UV observations from the Ultraviolet Imaging Telescope (UVIT) on board the AstroSat telescope (A. Kumar et al. 2012). UVIT consists of two coaligned Ritchey–Chrétien telescopes with a field of view of $0.^{\circ}5$, one for FUV (1300–1800 Å) and the other for NUV (2000–3000 Å) and visible (VIS) bands. We obtain Level 1 data from the Indian Space Science Data Centre (ISSDC) website.[6] The raw UVIT data is reduced following

[6] https://astrobrowse.issdc.gov.in/astro_archive/archive/Home.jsp

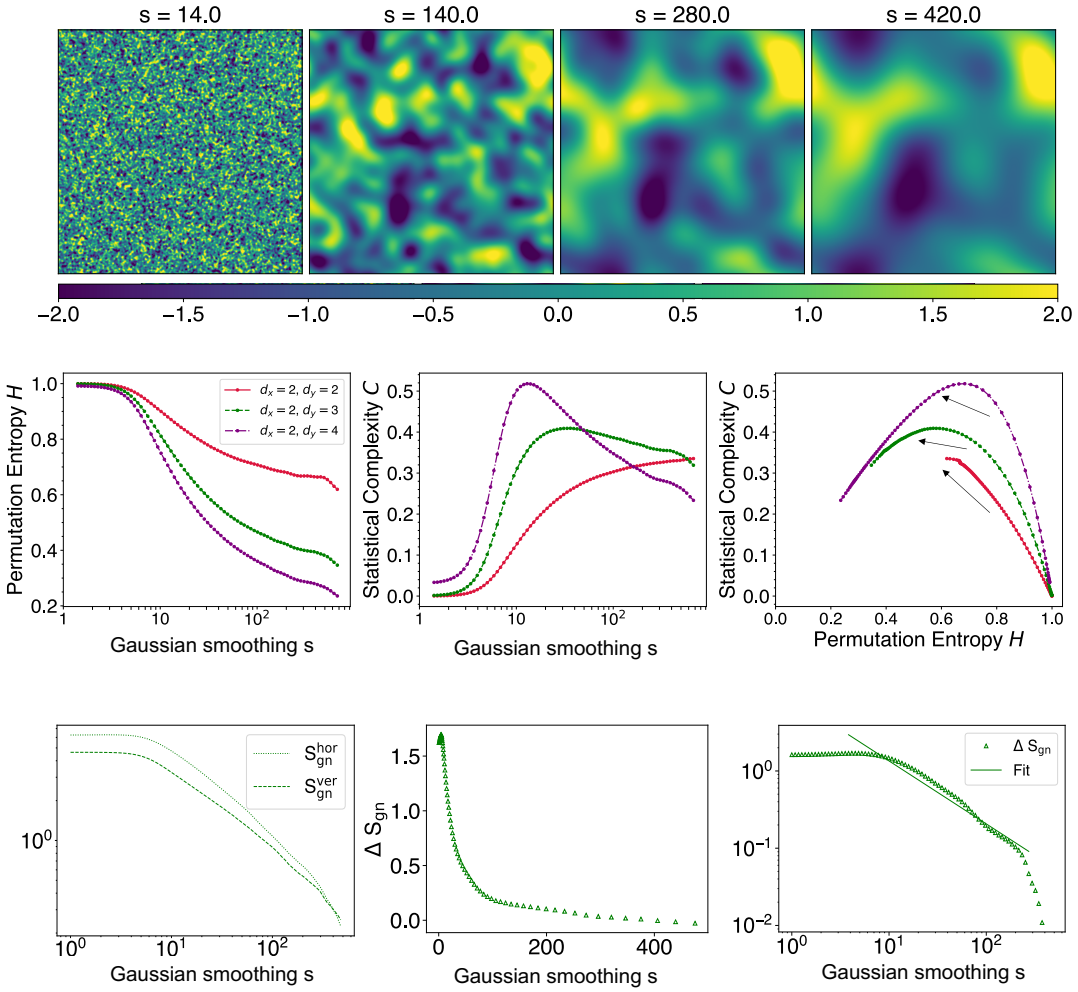

Figure 1. Top row: one realization of a 2D isotropic Gaussian random field generated on a grid of 500^2 pixels, with increasing smoothing scales (left to right) given in units of pixel numbers. Middle row: permutation entropy, H, (left) and statistical complexity, C, (middle), as functions of the smoothing scale s at embedding dimensions $(d_x, d_y) = (2, 2)$ (red), (2, 3) (green), and(2, 4) (purple), for the fields in the top row. The right panel shows the CH-plane. The black arrows indicate the direction of increasing s. Bottom row: horizontal, S_{gn}^{hor}, (dotted) and vertical, S_{gn}^{ver}, (dashed) global node entropies (left), global node entropy difference, ΔS_{gn}, (middle), as functions of the smoothing scale, for $(d_x, d_y) = (2, 3)$. The log–log plot of the right panel shows an inverse power-law fit (solid line) to ΔS_{gn} (triangles) as a function of smoothing scale.

S. Amrutha & M. Das (2025). Multiple filter observations are available for NGC 628. We use only the NUVB4 N263M filter (1365 s exposure time).

NGC 628 is a part of the Physics at High Angular Resolution in Nearby GalaxieS (PHANGS) program.[7] We use reduced archival data from the Atacama Large Millimeter/submillimeter Array (ALMA; A. K. Leroy et al. 2021a, 2021b) CO ($J = 2 \rightarrow 1$) moment 0 map and the James Webb Space Telescope (JWST; J. C. Lee et al. 2023) MIR instrument (MIRI) F2100W[8] and NIR camera (NIRCam) F360M images, both obtained from the PHANGS Treasury. Table 1 lists relevant image parameters for the data used in our study.

To ensure consistent spatial scales across all four images, we apply interpolation so that the plate size would cover the same area of the galaxy ($0\farcs417\,\mathrm{pix}^{-1}$). Each pixel corresponds to a physical size of 19.89 pc. We convolve all images to a common resolution of $1\farcs2$ (UVIT; the poorest resolution among the maps), corresponding to the physical scale of 57 pc. The final images, displayed in Figure 2(a), consist of 530×311 pixels, spanning $10.54 \times 6.19\,\mathrm{kpc}^2$.

3.2. Multiwavelength View of NGC 628

NUV. This emission traces recent star formation, predominantly from O, B, and massive A stars over timescales of 200–300 Myr (D. A. Thilker et al. 2005). In NGC 628, large NUV star-forming complexes are found in the wider arms and interarm regions. A faint UV emission is observed across the disk, especially at the galaxy's center, indicating some evolved stellar populations and scattered dust. NGC 628 has experienced self-regulated star formation over the last 500 Myr (R. H. Cornett et al. 1994; J. Zaragoza-Cardiel et al. 2019), owing to the lack of interactions in the past Gyr.

NIR (3.6 μm). This emission traces the bulk of low-mass stars and evolved giants (which have moved off the main sequence), producing smoother, less clumpy arms. The center is bright, with two prominent spiral arms and a visible bifurcation in the top-right arm.

MIR. The emission in MIR is due to re-emission of UV and visible light absorbed by the dust, tracing embedded star

[7] https://sites.google.com/view/phangs/home

[8] https://jwst-docs.stsci.edu/jwst-mid-infrared-instrument/miri-observing-modes/miri-imaging#gsc.tab=0

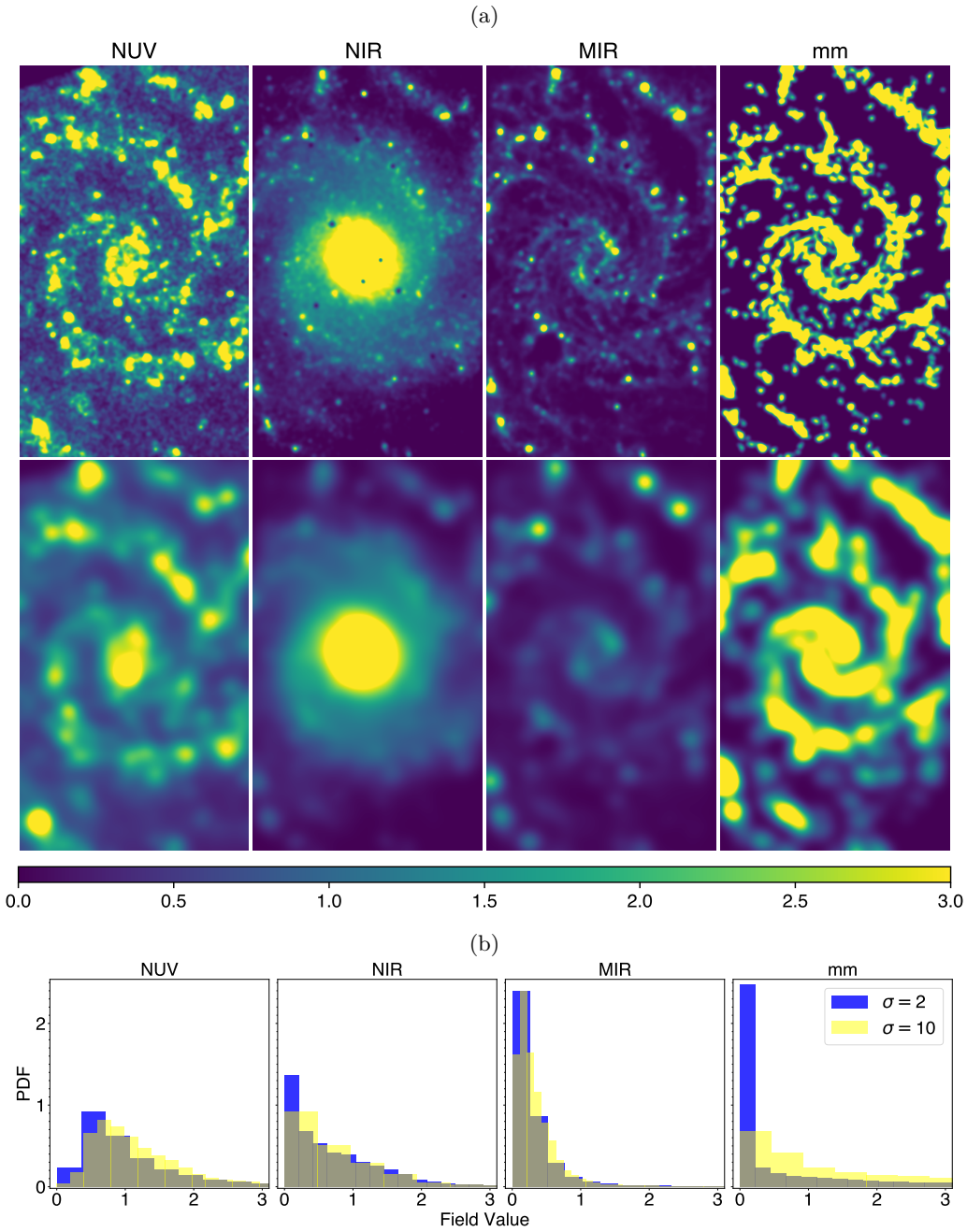

Figure 2. Top row of (a): images of the galaxy NGC 628 observed at NUV, NIR, MIR, and mm wavelengths (left to right) obtained from UVIT, JWST (NIR and MIR), and the Atacama Large Millimeter/submillimeter Array (ALMA), respectively. All images cover identical fields of view. The intensity values of each image have been normalized by the respective standard deviation. All images are smoothed identically using a Gaussian kernel with a smoothing scale $\sigma = 2$ (in pixels). Bottom row of (a): same as the top row but for $\sigma = 10$. Image parameters are provided in Table 1. (b) Probability density functions (PDFs) of the field values of the four images in (a) corresponding to the top row (blue), and bottom row (yellow).

Table 1
Image Parameters

Image	Central Wavelength (nm)	Image PSF (arcsec)	Platescale ($''$ pix^{-1})	Pixel Unit
UVIT NUV	2.63×10^2	1.2	0.417	counts
JWST NIR	3.6×10^3	0.12	0.063	MJy sr^{-1}
JWST MIR	2.1×10^4	0.67	0.11	MJy sr^{-1}
ALMA mm	1.3×10^6	1	0.2	K km s^{-1}

formation. The MIRI F2100W band (includes 24 μm) reveals bright spiral arms, spurs (T. G. Williams et al. 2022), bubbles (E. J. Watkins et al. 2023), and web-like interarm structures.

Millimeter (mm). The mm emission of our data corresponds to the $J = 2 \rightarrow 1$ transition of carbon monoxide (CO) molecules, which indirectly traces cold molecular hydrogen clouds that exhibit clumpy structures. With the ALMA strict map, diffuse emission is filtered out (A. K. Leroy et al. 2021a). CO emission is bright throughout the spiral arms and spurs.

3.3. Coarse-graining Images

To carry out a multiscale probe of the structural properties of NGC 628, we systematically perform coarse-graining (smoothening) of the multiwavelength images using Gaussian kernels with different standard deviations σ (in units of pixel numbers). Throughout this paper, we use "smoothing scale" to mean the standard deviation of the smoothing kernel. This process mimics telescope beam smoothing and enables analysis at varying resolutions. By varying σ, we study small- and large-scale morphological features arising from multiscale physical interactions. Figure 2(a) displays the images smoothed with $\sigma = 2$ (first row) and 10 (second row).

Effective physical scale. The point-spread function (PSF) values quoted in Table 1 are full-width at half maximum (FWHM) values. The common smoothing of all images by FWHM $1\farcs2$ corresponds to 57 pc in physical scale, and the corresponding smoothing scale is 24.2 pc. In pixel units, this corresponds to a smoothing scale, denoted by σ_a, of 1.22. Since the smoothing by σ discussed above is in addition to the common smoothing by σ_a, the effective smoothing scale, in pixel units, is

$$\sigma_{\rm eff} = \sigma\sqrt{1 + (\sigma_a/\sigma)^2}\,. \tag{17}$$

For $\sigma \gg \sigma_a$, we have $\sigma_{\rm eff} \sim \sigma$. Then the physical length scales, which we denote by $L_{\rm FWHM}$, associated with the FWHM value corresponding to $\sigma_{\rm eff}$ are given by

$$L_{\rm FWHM} = 2\sqrt{2\ln 2}\ \times\ \sigma_{\rm eff}\ \times\ 19.89\ {\rm pc}. \tag{18}$$

In Section 4 we will primarily use the smoothing scale σ for plotting and presenting our results, unless stated otherwise. However, for interpretation in terms of physical length scales, we will use $L_{\rm FWHM}$, which is the length corresponding to the smoothing FWHM.

3.4. Probability Distribution Functions at Multiwavelengths

The panels in Figure 2(b) show the probability density functions (PDFs) of the emissions of NGC 628 at NUV, NIR, MIR, and mm wavelengths, for smoothing scales $\sigma = 2$ (blue) and $\sigma = 10$ (yellow). We observe that all PDFs are right-skewed. For the mm image, we observe a sharp drop in the PDF values for lower field values. A precise modeling of the PDFs is not important for our discussion here.

4. Results for NGC 628

In this section, we present the results obtained for permutation entropy H, disequilibrium D_E, statistical complexity C, and ordinal network global node entropy $S_{\rm gn}$ for the multiwavelength images of NGC 628. We probe the multiscale nature by smoothing the galaxy field data at different scales σ and using different choices of embedding dimensions (d_x, d_y).

Choice of embedding dimensions. We use combinations of $(d_x, d_y) = (2, 2)$, $(2, 3)$, and $(2, 4)$. These choices are constrained by the total number of available pixels in the data, and the condition for statistical reliability: $(d_x d_y)! \ll 164,830$. Different embedding dimensions explore correlations for varying chunks of data, and this can potentially reveal distinct structural features that may not be apparent at a single embedding dimension.

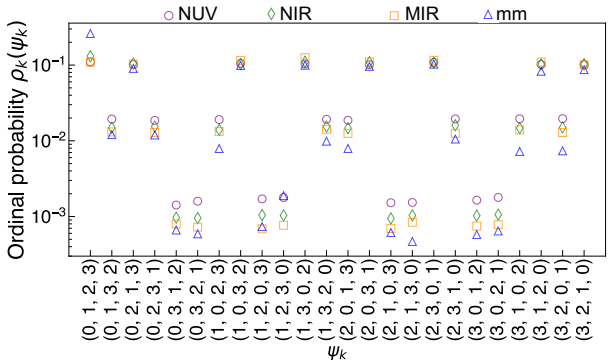

Figure 3. Ordinal probabilities $\{\rho_k(\psi_k)\}$ of the four NGC 628 images when $(d_x, d_y) = (2, 2)$ at smoothing scale $\sigma = 2$.

The numbers of distinct states, permutation states, and the physical sizes (each pixel rounded off to 20 pc) associated with the three (d_x, d_y) choices are listed as Table 2 below.

Table 2
Counts of Distinct and Permutation States, and Physical Sizes of Spatial Regions Corresponding to the Three Embedding Dimension Choices

(d_x, d_y)	No. of Distinct States	No. of Permutation States	Physical Size in pc^2
(2, 2)	24	163,990	40 × 40
(2, 3)	720	163,461	40 × 60
(2, 4)	40,320	162,932	40 × 80

As a demonstration, we present the ordinal probabilities $\{\rho_k(\psi_k)\}$ for the four images of NGC 628 at $\sigma = 2$ for $(d_x, d_y) = (2, 2)$ in Figure 3. The x-axis shows the 24 distinct states ψ_k. We see that some states are more probable than others. The manner in which the ordinal probabilities deviate from equiprobable distribution results in distinctive behavior of the statistical quantities (H, D_E, C, and $S_{\rm gn}$) introduced in Section 2.

Estimation of errors. We estimate errors associated with the computed values of H, D_E, and C values of NGC 628 as follows. We divide the data into 20 equally sized patches, each having an area roughly $2.11 \times 1.53\ {\rm kpc}^2$. Then, treating each patch as independent data, we compute H, D_E, and C, and treat the standard deviations from the 20 values as the statistical uncertainties. Note that this way of estimating errors will slightly underestimate the true errors since the different patches are actually correlated.

The errors in H and D_E will propagate to yield the error in C. To quantify this, let σ_H, σ_{D_E}, and σ_C denote the standard deviations (errors). Then,

$$\sigma_C^2 = \bar{D}_E\sigma_H^2 + \bar{H}\sigma_{D_E}^2 + 2\bar{H}\bar{D}_E{\rm Cov}(H, D_E), \tag{19}$$

where the bar indicates mean values, and ${\rm Cov}(H, D_E)$ is the covariance between H and D_E. Intuitively, we expect H and D_E to be anticorrelated, with ${\rm Cov}(H, D_E)$ being negative. We explicitly compute the covariance and confirm that this is so. Then, σ_C will not be simply related to the quadrature sum of σ_H and σ_{D_E}. For all results shown henceforth, we will use σ_H, σ_{D_E}, and σ_C to show the error bars.

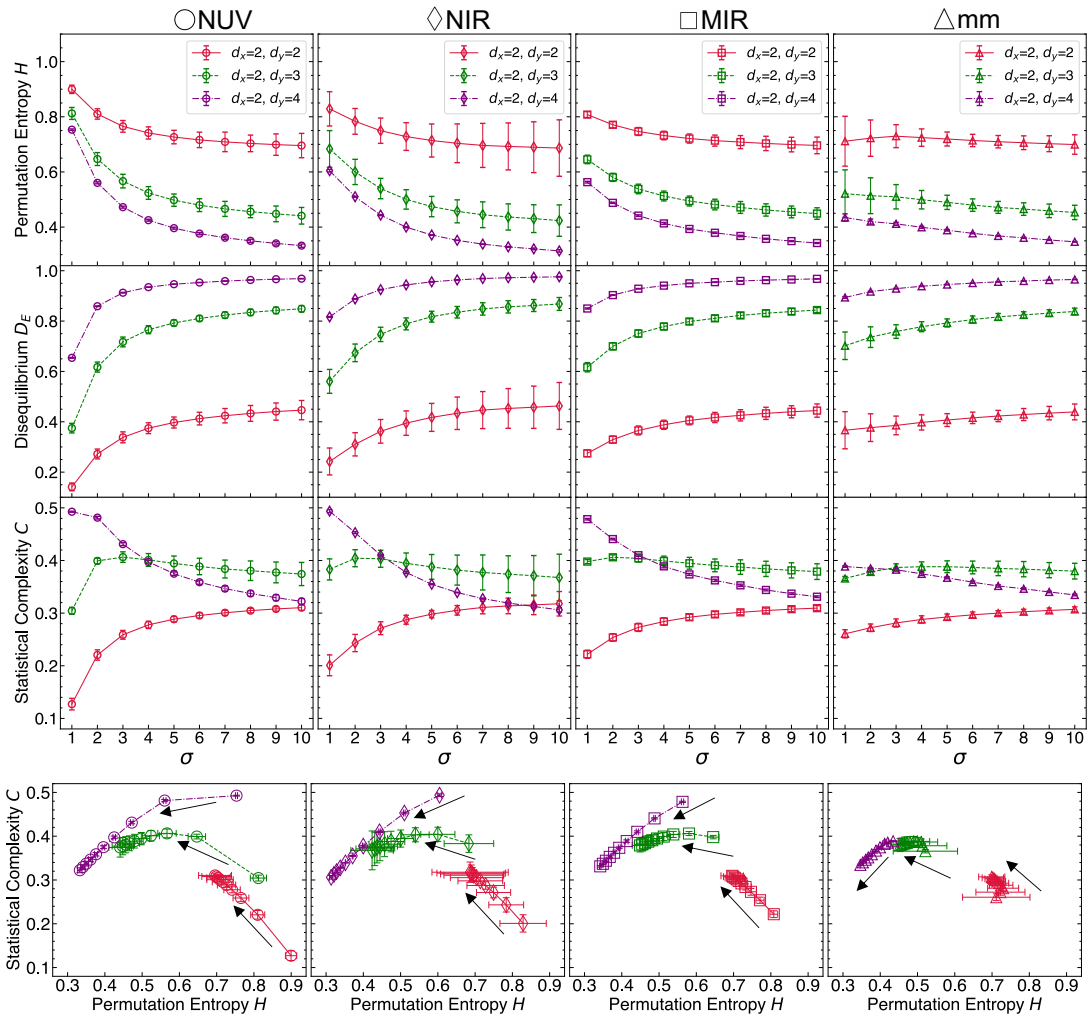

Figure 4. First, second, and third rows: H, D_E, and C computed using $(d_x, d_y) =$ (2, 2) (red), (2, 3) green, and (2, 4) (purple) for the four images of NGC 628 shown in Figure 2 smoothed at different scales σ (in units of 10 pc). The details of the images are provided in Table 1. Bottom row: values of C and H shown on the CH-causality plane for the three cases of (d_x, d_y) of the four NGC 628 images at different smoothing scales. The black arrows indicate the direction of increasing σ.

4.1. Entropy, Disequilibrium, and Complexity for Different Wavelength Images of NGG 628 across Scales

Figure 4 shows permutation entropy (H), disequilibrium (D_E), and statistical complexity (C) as functions of smoothing scale σ at $(d_x, d_y) = (2, 2)$, (2, 3) and (2, 4). From the top row, at all embedding dimensions (d_x, d_y), in all bands except mm, H decreases with increasing σ consistent with the loss of small-scale structures seen in the images: in NUV emission from evolved stellar population and dust scattering, in NIR due to starlight from low-mass stars, dust continuum, and scattered light, and in MIR from bright clumpy dust in the spiral arm, with diffuse interarm web structures. Since H quantifies randomness, diffuse structures in the observed data have a pronounced effect on H. At mm wavelength, however, H shows only mild variation with σ, reflecting the cold and clumpy nature of the emission and the lack of diffuse structures, as also evident in the PDFs of Figure 2(b), where mm and MIR have most of the field values around 0. A mild nonmonotonic behavior for $(d_x, d_y) = (2, 2)$ at small σ is further explained by the clumpy nature of regions that emit in mm wavelengths, making them less disordered. The second row shows increasing D_E with σ across all wavelengths and (d_x, d_y), indicating greater structural order as fluctuations are washed out with smoothing. The third row shows the behavior of C, encoding information of both H and D_E, with σ at different (d_x, d_y), highlighting that different embedding dimensions capture distinct aspects of the galaxy's complexity inherent in different spatial structures of the galaxy field at the given scale.

We observe that for H and D_E, $(d_x, d_y) = (2, 2)$ has the largest error bars, with a drop toward higher embedding dimensions across all wavelengths. The errors tend to increase with σ, except for mm, which shows the opposite trend. Moreover, NIR shows larger error bars relative to other wavelengths, indicating larger fluctuations across the galaxy. MIR shows the smallest error bars, indicating relative uniformity of the fluctuations across the galaxy. We also observe that for C the sizes of error bars do not follow the trends of H and D_E, which is because of Cov(H, D_E) being negative.

The bottom row of Figure 4 shows the CH-planes parameterized by σ, with the black arrows indicating increasing σ. Across different embedding dimensions, H consistently decreases with increasing smoothing for all images (except mm at $(d_x, d_y) = (2, 2)$). However, complexity C exhibits interesting behaviors: for $(d_x, d_y) = (2, 2)$, C shows increasing trends; for $(d_x, d_y) = (2, 4)$, C decreases; and for

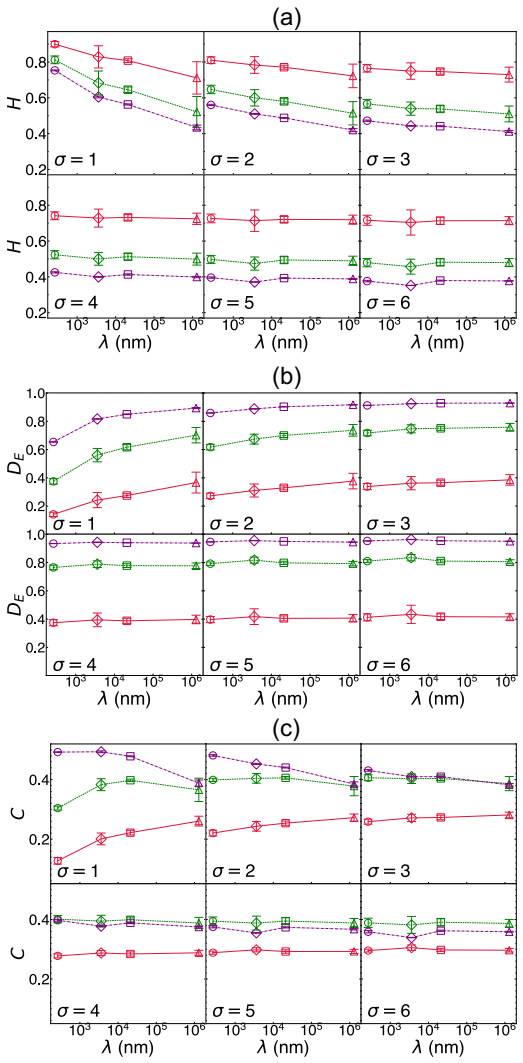

Figure 5. Comparison of H (a), D_E (b), and C (c) as functions of observing wavelength λ (in nanometers), for each smoothing scale.

$(d_x, d_y) = (2, 3)$, C follows nonmonotonic behaviors. Since C $(=D_E \times H)$ reflects the interplay between order (organization) and disorder (randomness), these variations of C reflect distinct complexity inherent in different spatial structures and scales of the galaxy. These results, therefore, highlight the morphological complexity of NGC 628 at multiscales.

4.2. Entropy, Disequilibrium, and Complexity of NGC 628 across Observing Wavelengths

We next examine how H, D_E, and C vary with observing wavelength λ. Figure 5 shows H, D_E, and C versus λ for $\sigma = 1, 2, \ldots, 6$. The markers and color codes are the same as in Figure 4. Figure 5 reveals two different behaviors in the variation of H, D_E, and C with σ for all λ. For scales $\sigma < 4$, H decreases with increasing wavelength for all embedding dimensions, as seen in panel (a). NUV has the highest entropy, which is explained by the fluctuating nature of star-forming regions across a wide range of spatial scales with diffuse emission in the entire disk. In comparison, there is a drop in diffuse emissions in NIR and further in MIR, resulting in lower values of H. The mm image has the lowest H value because the emissions primarily originate from cold, clumpy regions, with no diffuse emissions. Additionally, UV emission from massive star associations can photoionize the surrounding gas (W. D. Vacca et al. 1996), making fluctuations particularly prominent in the NUV band. Previous studies have also indicated that these associations drive large-scale motions, contributing to turbulence and structure in the interstellar medium (ISM; B. G. Elmegreen & J. Scalo 2004; S. Kim & C. Park 2007). Through stellar winds and supernova explosions, these stars inject energy (A. Maeder & P. S. Conti 1994), and create bubbles and superbubbles, ranging from a few parsecs to several kiloparsecs, which are evident in the JWST MIR observations of NGC 628 (A. T. Barnes et al. 2023; E. J. Watkins et al. 2023). However, for scales $\sigma \geqslant 4$, H does not significantly vary with the variation of wavelength, as both small-scale structures and diffuse emissions get washed out due to the effect of larger smoothing. Further examination of D_E and C also shows similar constant behavior as H for $\sigma \geqslant 4$.

Emergence of a transition scale. In Figures 6(a) and (b), we present the $D_E H$- and CH-planes, where data points corresponding to all four wavelengths (distinguished by different markers) are plotted together for each value of σ. We observe that, for all embedding dimensions, the values across the four wavelengths converge for $\sigma \geqslant 4$. This observation reinforces the conclusion drawn earlier from Figure 5. Hence, based on visual inspection, $\sigma = \sigma^{(c)} \sim 4$ emerges as a critical transition scale beyond which the degrees of order and disorder in NGC 628 exhibit universal behavior across all four wavelengths. Converting $\sigma^{(c)}$ to a physical scale, which we denote by $L^{(c)}_{\rm FWHM}$ using Equation (18), we obtain a value of 196 pc as the effective transition length scale. We note that this value is not precisely determined, and the uncertainty has not been rigorously quantified. However, a rough estimate using $L_{\rm FWHM}(\sigma = 3) \simeq 152$ pc gives an error of $[(196 - 152)/2]$ pc, which is 22 pc. Hence, the uncertainty must be around 10%. For this reason, we quote the value of $L^{(c)}_{\rm FWHM}$ to be of the order of $\sim$200 pc.

Physical significance of the transition scale. At scales below $L^{(c)}_{\rm FWHM}$, NUV has the highest H and lowest D_E, with decrease/increase of H/D_E toward higher wavelengths. This trend supports the physical expectation that UV photons generated by stars transfer energy to the ISM, and have a cascading (but delayed in terms of a shift in the values of H and D_E) effect. There exists a hierarchy of scales related to star clusters such as OB associations and stellar aggregates (see, e.g., A. S. Gusev 2014), and characteristic scales associated with distinct features of the ISM such as clumps and holes related to stellar winds, supernova bubbles and superbubbles (arising from multiple supernova explosions; S. Kim & C. Park 2007). The hierarchy of these scales is revealed as the increasing/decreasing part of the plots of H/D_E versus σ. At $L^{(c)}_{\rm FWHM}$ and higher, all wavelengths share the same values of H and D_E, implying that they trace the same structural features. Therefore, $L^{(c)}_{\rm FWHM} \sim 200$ pc captures the transition from scales affected by star formation and stellar feedback, to larger scales where the galaxy's morphology is shaped by global gravitational dynamics.

Emergence of attractor curves. Figure 6(c) shows the values of C and H for all wavelengths (distinguished by markers) across smoothing scales, plotted on a common CH-plane. The progression toward lighter colors indicates increasing smoothing scales, as shown by the color bars at the bottom. We see that C and H values tend to align along the same curve at each (d_x, d_y), except the mm image toward small σ. This suggests the existence of an *attractor curve* for NGC 628, for each

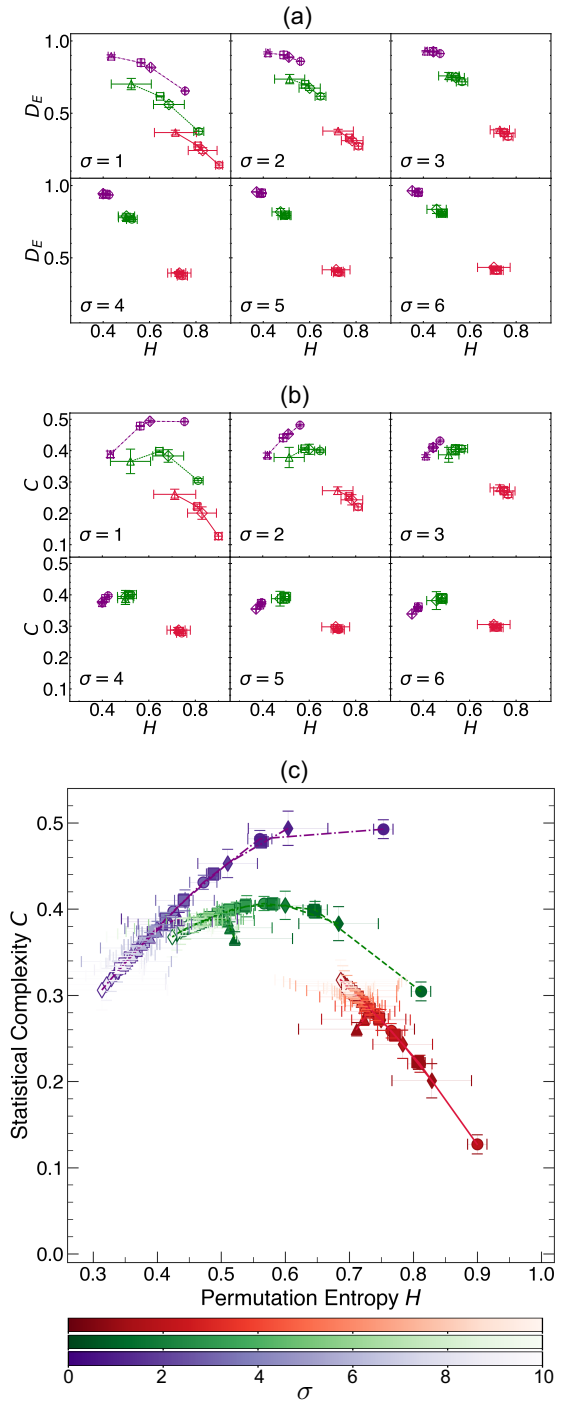

Figure 6. (a) D_E vs. H for the four images of NGC 628 shown in the same panel (same markers as Figure 5), for different σ and (d_x, d_y). (b) *CH*-plane for different σ. (c) C and H values for all wavelengths and σ are plotted on the same *CH*-plane. The color bars at the bottom indicate larger σ toward lighter hues.

(d_x, d_y). It is noteworthy that for the smallest embedding dimension, H and C span relatively smaller regions of the phase space, indicating that larger embedding dimensions are necessary to better probe the structural components of the galaxy.

Further, we generate GRFs with power spectra of the form $P(k) \propto k^{-n}$, where $n = 0, 1, 2,$ and 3. The three light-colored *CH*-curves on each panel of Figure 7(a) represent the (H, C) values of smoothed GRFs (parameterized by s and increasing in the same direction as σ) for fixed seeds corresponding to the three embedding dimensions. In each panel, we use the same markers and colors (indicated by the color bar) as in Figure 6(c) for the four wavelength images. We do not make a comparison between s and σ since the GRF is not a physical field, and we cannot compare the pixel sizes directly. What is of interest to observe is that the *CH*-trajectories of the GRFs with $n = 1$ align most closely with those of the NGC 628 galaxy field, indicating that the galaxy field shares similar correlation properties with a pink-noise $(1/f)$ spectrum. It further suggests an underlying universality of the attractor curves, despite the differing physical processes traced by each wavelength.

Robustness of our results. To test the effect of rotation of the data, we repeat all calculations for the four image data, as well as the GRFs, after interchanging d_x and d_y (except (2, 2), which is symmetric). We find a negligible effect of the rotations on all of the results. We note that the results would remain invariant to any order-preserving transformation of the data, since the ordinal distributions are the same.

4.3. Surrogate Analysis as a Control Study to Quantitatively Determine the Transition Scale

Next, to test whether the galaxy's *CH*-curve is determined solely by its power spectrum, we construct realizations of phase-randomized surrogate GRFs for each wavelength and smoothing scale σ. These surrogates preserve the exact power spectrum of the galaxy but have randomized Fourier phases, thereby destroying nonlinear correlations while retaining all linear correlations. Further justification on constructing these phase-randomized surrogates is provided in Appendix B. In Figure 7(b), we show the mean (H, C) results (indicated by markers and colors at the top of the panel) obtained from 60 realizations of surrogate fields (with error bars) along with the galaxy results. The three panels in the bottom row show the zoomed-in views of the boxed regions. Black arrows indicate the direction of increasing σ. For $(d_x, d_y) = (2, 2)$ (right panel), the phase-randomized surrogates track the galaxy data reasonably well, indicating that low-dimensional embeddings are dominated by linear correlations, which the power spectrum captures. However, for $(d_x, d_y) = (2, 3)$ (middle panel) and (2, 4) (left panel), the (H, C) values of the surrogate fields begin deviating from the galaxy curve already at small σ, and the deviation becomes particularly strong around $\sigma \sim 4$. This further demonstrates that $\sigma = \sigma^{(c)} \sim 4$ marks a critical transition scale, where nonlinear, phase-dependent correlations present in the galaxy data are no longer reproduced by Gaussian surrogates that match the power spectrum. We interpret the results as follows. Below $\sigma < \sigma^{(c)}$, surrogates lie close to the galaxy curve, and much of the small-scale structure is consistent with what the power spectrum captures for small (d_x, d_y). Nonlinear correlations (turbulence, fractal hierarchy) exist to cause significant deviations for larger (d_x, d_y). Around $\sigma = \sigma^{(c)}$, surrogates begin to deviate significantly, marking the emergence of nonlinear, phase-dependent correlations that cannot be captured by the power spectrum alone. For $\sigma > \sigma^{(c)}$, deviations grow substantially. These scales reflect coherent galactic morphology, requiring a phase-organized structure that Gaussian surrogates cannot reproduce. We note that for NIR, $\sigma^{(c)} \sim 5$ and its *CH*-curve appears different as compared to the other wavelengths that trace younger stellar populations and molecular gas. Older populations are, in general, more dispersed and form larger

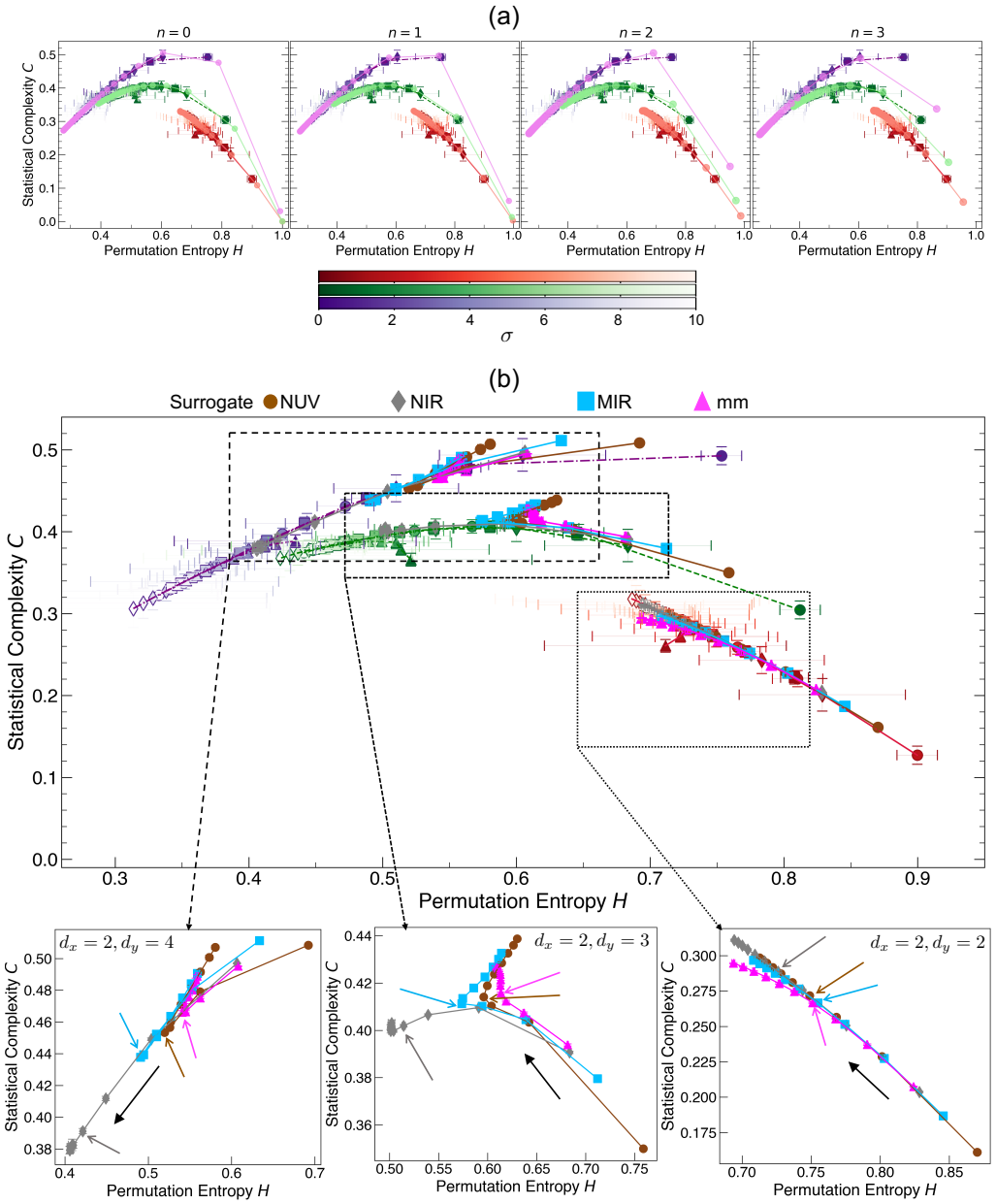

Figure 7. (a) *CH*-planes for comparison between the four wavelength images of NGC 628 and GRFs with power spectra of the form $P(k) \propto k^{-n}$ with $n = 0$, 1, 2, and 3. In each panel, we use the same markers and colors (indicated by the color bar) as in Figure 6(c) for the four wavelengths, whereas the lighter-colored curves now correspond to the GRFs at the three different embedding dimensions $(d_x, d_y) = (2, 2)$, (2, 3) and (2, 4). (b) Surrogate fields: in the upper panel, we plot the (C, H) values of the four images of NGC 628 along with the corresponding plots for the surrogate fields (indicated by different markers and colors at the top of the panel). Each surrogate field is a GRF constructed by preserving the power spectrum of the galaxy and randomizing the Fourier phases, at each wavelength and smoothing scale σ. The bottom panels show the zoomed-in views of the above boxed regions, showing the (C, H) values of the surrogate fields only (for visual clarity) at the three different embedding dimensions $(d_x, d_y) = (2, 2)$, (2, 3) and (2, 4). In the panels, each point on the *CH*-plane corresponds to σ values from 1–10 (increasing in the direction indicated by the bold black arrows) for a given surrogate field (same marker and color). Colored arrows (brown, gray, light blue, and pink) indicate where $\sigma = 4$ is located.

complexes (B. G. Elmegreen et al. 2006). An additional bright, large structure at the center for NIR might be the reason behind the observed difference.

The transition scale $\sigma^{(c)} \sim 4$ is consistent with the correlation length, $l_{\rm corr}$, inferred using the two-point correlation function for NGC 628 (K. Grasha et al. 2017; S. H. Menon et al. 2021). These studies interpret $l_{\rm corr}$ as the maximum separation over which star clusters remain correlated in the scale-free, turbulent fractal hierarchy generated by star formation and stellar feedback. Beyond this scale, the fractal hierarchy breaks down, and large-scale gravitational dynamics begin to shape global morphology. For a spiral galaxy like NGC 628, $l_{\rm corr}$ marks the shift from a fractal distribution influenced by turbulence to larger scales, where galactic dynamics dominate. Thus, below ∼200 pc, the galaxy contains strong turbulent, fractal, nonlinear correlations, whereas above ∼200 pc, the structure transitions to large-scale, phase-organized morphology that cannot be reproduced by Gaussian fields. The close agreement between $L^{(c)}_{\rm FWHM}$ and $l_{\rm corr}$ supports the interpretation that ∼200 pc represents a fundamental physical transition scale in NGC 628: the boundary between turbulence-driven small-scale structure and large-scale galactic organization.

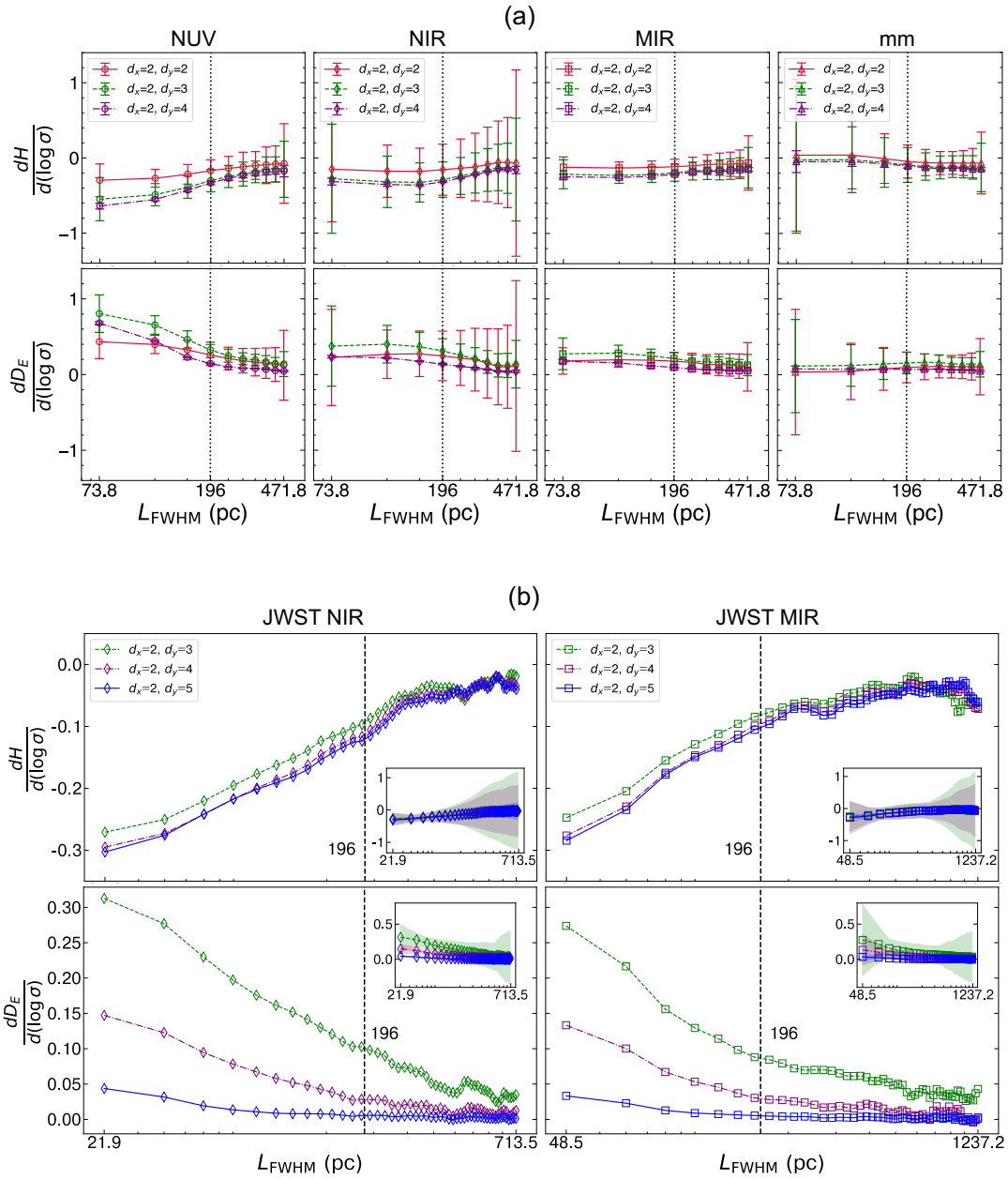

Figure 8. (a) $dH/d(\log\sigma)$ and $dD_E/d(\log\sigma)$ vs. $L_{\rm FWHM}$ for the four images of NGC 628. The black dotted vertical line marks $L^{(c)}_{\rm FWHM} = 196$ pc. (b) Similar plots as in (a) but for high-resolution JWST NIR and MIR images. Insets display the corresponding plots with error bars shown as colored shaded regions. Embedding dimensions are indicated in the legend.

4.4. Disorder to Order Transition for Individual Wavelength Images of NGC 628 and High-resolution JWST NIR and MIR Images

The value of $\sigma^{(c)}$ quoted in the previous subsections is inferred from the comparative behavior of H, D_E, and C across wavelengths as a function of σ as well as surrogate analysis. Since the scale dependence varies across individual wavelengths, we further analyze the slopes of H and D_E with respect to $\log\sigma$ for each wavelength, as shown versus $L_{\rm FWHM}$ in Figure 8(a). These plots reveal significant variation among the wavelengths, indicating that the observed emissions arise from a mix of physical processes, each dominating at different spatial scales.

The original JWST NIRCam F360M and MIRI F2100W images have plate scales 3 pc and 5.2 pc, respectively, compared to the 19.89 pc used previously. We recompute H and D_E using full-resolution data (see Table 1 for angular resolution) over a broader range of smoothing scales than in Figure 8(a), enabling finer-scale fluctuation detection. With pixel number of the order of $\sim 10^6$, we now use $(d_x, d_y) = (2, 3)$, $(2, 4)$, and $(2, 5)$. The resulting slopes are shown in Figure 8(b), with uncertainties indicated by the shaded regions in the insets.

While the plots in panel (b) are qualitatively similar to the corresponding NIR and MIR results in Figure 8(a), they also reveal notable differences that reflect the added sensitivity to small-scale structures. Interestingly, in both NIR and MIR, the slopes of H and D_E flatten and show oscillations on scales larger than 200 pc. This behavior at high σ may reflect statistical fluctuations induced by large-scale galactic

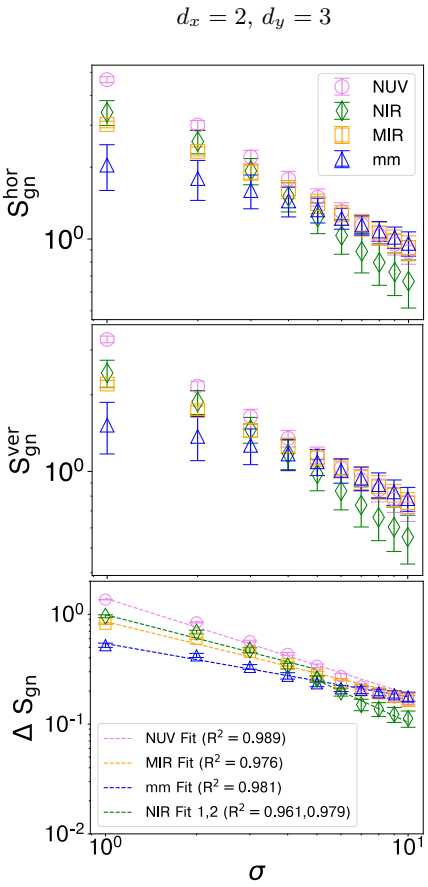

Figure 9. Variation of global node entropy S_{gn} with smoothing scale σ for embedding dimension $(d_x, d_y) = (2, 3)$: Horizontal global node entropy, S_{gn}^{hor} (top panel), vertical global node entropy, S_{gn}^{ver} (middle panel), global node entropy difference, $\Delta S_{gn} = S_{gn}^{hor} - S_{gn}^{ver}$, (bottom panel) vs. σ on log–log plots. In the bottom panel, dashed lines represent inverse power-law fits ($\Delta S_{gn}(\sigma) = a\sigma^{-b}$) with corresponding R^2-values for the goodness of fit (indicated in the legend). Values of power-law exponents b are: 0.8705 (NUV), 0.6730 (MIR), and 0.4854 (mm). For NIR, we have fitted in two regimes with $b = 0.7133$ and 1.2793.

structures. Additionally, the associated uncertainties increase with σ, due to the reduced number of independent regions at larger smoothing scales. The important thing to be noticed is that the embedding dimensions cover a much smaller physical scale in Figure 8(b) compared to Figure 8(a). Hence, small embedding dimensions show more fluctuations at the same large smoothing scales. These fluctuations may also stem from variations in structure size with galactocentric distance, as some large features appear in the galaxy's outskirts. However, this study is limited to the inner disk of NGC 628.

4.5. Ordinal Network Global Node Entropy S_{gn} across Scales

We map the multiwavelength NGC 628 images at different σ (in pixel units) into horizontal and vertical ordinal networks. We compute the corresponding horizontal (S_{gn}^{hor}) and vertical (S_{gn}^{ver}) global node entropies, and their difference ($\Delta S_{gn} = S_{gn}^{hor} - S_{gn}^{ver}$) using $(d_x, d_y) = (2, 3)$ (Figure 9). The decrease of S_{gn}^{hor}, S_{gn}^{ver}, and ΔS_{gn} with σ indicates progressive loss of the overall structural information of the galaxy field with smoothing. We again fit inverse power-law functions (dashed lines): $\Delta S_{gn}(\sigma) = a\sigma^{-b}$ to the data (markers), with exponents: $b = 0.8705$ (NUV), 0.6730 (MIR), and 0.4854 (mm; R^2-values indicated in the legend). Entropy decays quickly in NUV (as the structures in this emission seem relatively even without strong clustering), slowly in mm (structures persist across scales with strong clustering), and moderately in MIR (some clustering exists, but not as pronounced as in mm). For NIR, two σ regimes emerge: $b = 0.7133$ for $\sigma < 5$, and $b = 1.2793$ for $\sigma \geqslant 5$, suggesting a transition from a relatively uniform distribution of low-mass stars at small scales to central bulk emission at larger scales. This result from the ordinal network global node entropies also supports the critical transition scale $\sigma^{(c)}$ observed for NIR in the preceding subsection.

The observed negative power-law decay of $\Delta S_{gn}(\sigma)$ in NGC 628 indicates a scale-free reduction of structural information, pointing to a hierarchical organization (A.-L. Barabási & R. Albert 1999) in the distribution of structures across scales. This hierarchical organization likely emerges from the self-organization (P. Bak et al. 1988) of various physical processes at multiple scales of the galaxy NGC 628, reflecting its multiscale complexity.

5. Conclusions

This study presents a novel approach to understanding the morphological complexity of the galaxy NGC 628 through the lens of statistical physics of complex systems. We demonstrate how the structural features of NGC 628 can be characterized within the framework of complexity analysis applied to empirical data. Using publicly available multiwavelength imaging data, we systematically analyze NGC 628's morphology across UV, NIR, MIR, and mm wavelengths, probing multiple physical scales. Our analysis employs the framework of ordinal patterns—permutation entropy, disequilibrium, statistical complexity, and ordinal network-based metrics. Taking into account a common field of view—set by the JWST MIR image—and the lowest resolution determined by the UVIT image—for the four images of NGC 628, our analysis probes smoothing scales ranging from 74–472 pc, corresponding to a physical extent of approximately 10 kpc.

Our first key finding is the emergence of a characteristic scale near 200 pc, where all structural complexity measures—permutation entropy, disequilibrium, statistical complexity, and global node entropy—show a clear transition. Surrogate field analysis (Figure 7(b)) further confirms the emergence of this transition scale, marking a shift in the ISM from fluctuations caused by the turbulence acting at the smaller scale to more self-organized structures influenced by galaxy dynamics and global gravitational instability, consistently across all embedding dimensions. The 200 pc scale aligns with the l_{corr}, indicating a physical connection and also lends support to the robustness of our method. Our approach quantitatively captures the impact of star formation, traced by UV emission, in driving ISM turbulence and enhancing spatial randomness. This effect is weaker in colder, clumpier CO-dominated regions. Beyond 200 pc, morphological differences across wavelengths become negligible.

Our second main conclusion is that the values of C and H for the four NGC 628 wavelengths trace a single smooth curve on the complexity-entropy plane, which asymptotes toward an "attractor" trajectory associated with isotropic GRFs. This suggests a statistically isotropic spatial distribution of the structures in NGC 628.

This pilot study demonstrates the effectiveness of ordinal patterns in probing the internal structure of galaxies and linking it to their nonequilibrium statistical states. A natural next step is to extend this analysis to a larger, morphologically diverse galaxy sample. Such a study could identify both distinguishing features for galaxy classification and underlying universal properties. This approach may also be combined with established geometrical and topological methods to uncover finer structural details; e.g., a topological analysis of HI in the Large Magellanic Cloud (S. Kim & C. Park 2007) revealed four characteristic scales, each associated with distinct features, clumps, or holes, arising from different physical processes. While our ordinal pattern framework captures structural transition scales, it does not yet differentiate between topological types like holes or clumps or even structures from the star formation hierarchy (A. S. Gusev 2014). Incorporating such distinctions is a direction we plan to pursue in future work.

Our findings may be viewed within a broader cosmological context. On sufficiently large scales, the cosmological density field is well approximated by a GRF, and its statistical properties are therefore fully described by the power spectrum. As gravitational instability drives nonlinear structure formation, mode coupling generates phase correlations, leading to coherent filamentary and clustered structures that cannot be captured by second-order statistics alone. Our results suggest that for galaxies, an opposite scale dependence may operate: at sufficiently small spatial scales, the surrogate and original galaxy images remain close in the complexity-entropy plane, indicating that local structure is largely consistent with the information encoded in the power spectrum. At scales around $\sigma = \sigma^{(c)}$, however, significant deviations emerge, marking the dominance of nonlinear, phase-dependent correlations. This behavior is consistent with a picture in which phase correlations are most significant in the nonlinear regime of structure formation in the Universe, wherein both very large and very small scales exhibit statistics closer to Gaussian behavior.

Acknowledgments

We thank the referees for carefully reading the manuscript and giving valuable comments and suggestions. A.L.C. acknowledges the APCTP (JRG program) through the Science and Technology Promotion Fund and Lottery Fund of the Korean Government and the Korean Local governments-Gyeongsangbuk-do Province and Pohang City. C.B.P. is supported by KIAS Individual Grants (PG016903) at the Korea Institute for Advanced Study, and the National Research Foundation of Korea (NRF) grant funded by the Korean government (MSIT; RS-2024-00360385).

This publication uses data from the UVIT, which is part of the AstroSat mission of the Indian Space Research Organisation (ISRO), archived at the Indian Space Science Data Centre (ISSDC). We gratefully thank all of the members of various teams for supporting the project from the early stages of design to launch and observations in orbit.

This work is based on observations made with the NASA/ESA/CSA JWST. The data were obtained from the Mikulski Archive for Space Telescopes at the Space Telescope Science Institute, which is operated by the Association of Universities for Research in Astronomy, Inc., under NASA contract NAS 5-03127. The observations are associated with the JWST program 2107. The specific JWST observation analyzed can be accessed via doi:10.17909/q9f5-zy15. This paper makes use of the following ALMA data: ADS/JAO.ALMA#2012.1.00650. S. ALMA is a partnership of ESO (representing its member states), NSF (USA), and NINS (Japan), together with NRC (Canada), MOST and ASIAA (Taiwan), and KASI (Republic of Korea), in cooperation with the Republic of Chile. The Joint ALMA Observatory is operated by ESO, AUI/NRAO, and NAOJ. The National Radio Astronomy Observatory is a facility of the National Science Foundation operated under a cooperative agreement by Associated Universities, Inc.

Facilities: Astrosat (UVIT), JWST, ALMA.

Software: astropy (Astropy Collaboration et al. 2013, 2018).

Appendix A
Illustration of the Construction of Ordinal Patterns

Let us consider a trivial example where the data Y is a 3×3 matrix given by

$$Y = \begin{pmatrix} 4 & 9 & 5 \\ 0 & 2 & 7 \\ 2 & 6 & 5 \end{pmatrix}. \tag{A1}$$

For ease of writing, the data elements are taken to be integers. The actual galaxy data we analyze is real-valued.

Let $d_x = 2 = d_y$ with unit embedding delay. Then $n_x = 2$, $n_y = 2$, which gives four submatrices. The steps of flattening each submatrix y to a sequence z, mapping z to a symbolic sequence A, sorting z to get z_S, and then obtaining the permuted symbolic sequence A_S, are explicitly demonstrated in Table A1 below.

We get four permutation states (ordinal patterns), which are given by the symbolic sequences A_S. These constitute the ordinal sequence $\{\pi_i^j\}$. Note that $(d_x d_y)! = 4!$ gives 24 possible distinct basis states (ψ_k). The number of elements of $\{\pi_i^j\}$ is <24 because Y is 3×3, which violates the requirement $d_x \ll N_x$, $d_y \ll N_y$ with $N_x = 3 = N_y$.

Table A1
Demonstration of the Ordinal Sequence Construction for the Matrix Y in Eq. A1.

Submatrix	Flatten and map to symbolic sequence		Sort and permute
$y = \begin{pmatrix} 4 & 9 \\ 0 & 2 \end{pmatrix} \Rightarrow$	$z = (4, 9, 0, 2)$ $A = (0, 1, 2, 3)$	$\Rightarrow$	$z_S = (0, 2, 4, 9)$ $A_S = (2, 3, 0, 1)$
$y = \begin{pmatrix} 9 & 5 \\ 2 & 7 \end{pmatrix} \Rightarrow$	$z = (9, 5, 2, 7)$ $A = (0, 1, 2, 3)$	$\Rightarrow$	$z_S = (2, 5, 7, 9)$ $A_S = (2, 1, 3, 0)$
$y = \begin{pmatrix} 0 & 2 \\ 2 & 6 \end{pmatrix} \Rightarrow$	$z = (0, 2, 2, 6)$ $A = (0, 1, 2, 3)$	$\Rightarrow$	$z_S = (0, 2, 2, 6)$ $A_S = (0, 1, 2, 3)$
$y = \begin{pmatrix} 2 & 7 \\ 6 & 5 \end{pmatrix} \Rightarrow$	$z = (2, 7, 6, 5)$ $A = (0, 1, 2, 3)$	$\Rightarrow$	$z_S = (2, 5, 6, 7)$ $A_S = (0, 3, 2, 1)$

Appendix B
Motivation of Surrogate Analysis

We now explain the statistical motivation of the surrogate analysis presented in Section 4.3. The constructed surrogate fields are GRFs that preserve the power spectrum of the galaxy while randomizing Fourier phases. Since the power spectrum determines the second-order statistics or two-point correlation

function of a stationary random field, these surrogates retain all second-order statistical properties of the original galaxy image, including variance and correlation length. On the other hand, randomizing the phase removes higher-order dependencies in the data structure, yielding a GRF that is consistent with the same power spectrum as the original image. Any systematic deviation of the permutation entropy or statistical complexity from the surrogate ensemble, therefore, indicates the presence of higher-order spatial organization beyond that encoded in the power spectrum. Thus, constructing galaxy surrogates that preserve the exact galaxy power spectrum but have randomized Fourier phases would be an objectively appropriate procedure for detecting transition scales in a given galaxy image.

ORCID iDs

Athokpam Langlen Chanu https://orcid.org/0000-0002-5071-7371
S. Amrutha https://orcid.org/0009-0005-6072-9252
Pravabati Chingangbam https://orcid.org/0000-0002-7385-8273
Changbom Park https://orcid.org/0000-0001-9521-6397

References

Amrutha, S., & Das, M. 2025, ApJ, 987, 11
Anand, G. S., Lee, J. C., Van Dyk, S. D., et al. 2020, MNRAS, 501, 3621
Aschwanden, M. 2011, Self-organized Criticality in Astrophysics: The Statistics of Nonlinear Processes in the Universe (Springer Science & Business Media)
Astropy Collaboration, Price-Whelan, A. M., Sipőcz, B. M., et al. 2018, AJ, 156, 123
Astropy Collaboration, Robitaille, T. P., Tollerud, E. J., et al. 2013, A&A, 558, A33
Bak, P., Tang, C., & Wiesenfeld, K. 1988, PhRvA, 38, 364
Balasis, G., Donner, R. V., Potirakis, S. M., et al. 2013, Entrp, 15, 4844
Bandt, C., & Pompe, B. 2002, PhRvL, 88, 174102
Barabási, A.-L., & Albert, R. 1999, Sci, 286, 509
Barnes, A. T., Watkins, E. J., Meidt, S. E., et al. 2023, ApJL, 944, L22
Bartlett, S., Li, J., Gu, L., et al. 2022, NatAs, 6, 387
Cano-Díaz, M., Ávila-Reese, V., Sánchez, S. F., et al. 2019, MNRAS, 488, 3929
Chanu, A. L., Park, Y., Cha, Y., et al. 2025, arXiv:2503.19924
Chanu, A. L., Singh, R. B., & Jeon, J.-H. 2024, CSF, 185, 115138
Connolly, A. J., Szalay, A. S., Bershady, M. A., Kinney, A. L., & Calzetti, D. 1995, AJ, 110, 1071
Conselice, C. J. 2006, MNRAS, 373, 1389
Consolini, G., Tozzi, R., & De Michelis, P. 2009, A&A, 506, 1381
Cornett, R. H., O'Connell, R. W., Greason, M. R., et al. 1994, ApJ, 426, 553
Cover, T. M. 1999, Elements of Information Theory (Wiley)
De Vaucouleurs, G. 1959, Classification and Morphology of External Galaxies (Springer), 275
de Vaucouleurs, G., de Vaucouleurs, A., Corwin, H. G., Jr., et al. 1991, Third Reference Catalogue of Bright Galaxies (NADS) (Springer)
Elmegreen, B. G., Elmegreen, D. M., Chandar, R., Whitmore, B., & Regan, M. 2006, ApJ, 644, 879
Elmegreen, B. G., & Scalo, J. 2004, ARA&A, 42, 211
Fiore, F., Gaspari, M., Luminari, A., Tozzi, P., & De Arcangelis, L. 2024, A&A, 686, A36
Friedrich, R., Peinke, J., Sahimi, M., & Tabar, M. R. R. 2011, PhR, 506, 87
Gekelman, W., Tang, S., DeHaas, T., et al. 2019, PNAS, 116, 18239
Gilbert, G. J., & Fabrycky, D. C. 2020, AJ, 159, 281
Gott, J. R., III, & Thuan, T. X. 1976, ApJ, 204, 649
Graham, A. W., & Driver, S. P. 2005, PASA, 22, 118
Grasha, K., Calzetti, D., Adamo, A., et al. 2017, ApJ, 840, 113
Gusev, A. S. 2014, MNRAS, 442, 3711
Hubble, E. P. 1936, Realm of the Nebulae (Yale Univ. Press)
Hyman, S. Ó., Daniel, K. J., & Schaffner, D. A. 2025, ApJ, 987, 195
Kamphuis, J., & Briggs, F. 1992, A&A, 253, 335
Karbashewski, S., Sydora, R., Van Compernolle, B., Simala-Grant, T., & Poulos, M. 2022, PhPl, 29, 112309
Kauffman, S. A. 1993, The Origins of Order: Self-Organization and Selection in Evolution (Oxford Univ. Press)
Kim, S., & Park, C. 2007, ApJ, 663, 244
Kreckel, K., Faesi, C., Kruijssen, J. M. D., et al. 2018, ApJL, 863, L21
Kumar, A., Ghosh, S. K., Hutchings, J., et al. 2012, SPIE, 8443, 84431N
Lang, P., Meidt, S. E., Rosolowsky, E., et al. 2020, ApJ, 897, 122
Langlen Chanu, A., Chingangbam, P., Rahman, F., Brojen Singh, R., & Kharb, P. 2024, JPCom, 5, 015005
Lee, J. C., Sandstrom, K. M., Leroy, A. K., et al. 2023, ApJL, 944, L17
Leroy, A. K., Hughes, A., Liu, D., et al. 2021a, ApJS, 255, 19
Leroy, A. K., Sandstrom, K. M., Lang, D., et al. 2019, ApJS, 244, 24
Leroy, A. K., Schinnerer, E., Hughes, A., et al. 2021b, ApJS, 257, 43
Lintott, C., Schawinski, K., Bamford, S., et al. 2011, MNRAS, 410, 166
Lloyd, S. 2001, ICSyM, 21, 7
Lopez-Ruiz, R., Mancini, H. L., & Calbet, X. 1995, PhLA, 209, 321
Lotz, J. M., Primack, J., & Madau, P. 2004, AJ, 128, 163
Lovallo, M., & Telesca, L. 2011, JSMTE, 2011, P03029
Maeder, A., & Conti, P. S. 1994, ARA&A, 32, 227
Mandelbrot, B. B. 1985, PhyS, 32, 257
Mao, X., Shang, P., & Li, Q. 2019, NonDy, 96, 2449
Martin, M., Plastino, A., & Rosso, O. 2003, PhLA, 311, 126
McCullough, M., Small, M., Iu, H., & Stemler, T. 2017, RSPTA, 375, 20160292
Menon, S. H., Grasha, K., Elmegreen, B. G., et al. 2021, MNRAS, 507, 5542
Morel, C., & Humeau-Heurtier, A. 2021, PaReL, 150, 139
Pessa, A. A., & Ribeiro, H. V. 2019, PhRvE, 100, 042304
Pessa, A. A., & Ribeiro, H. V. 2020, PhRvE, 102, 052312
Pessa, A. A., & Ribeiro, H. V. 2021, Chaos, 31, 063110
Poggianti, B. M., Fasano, G., Bettoni, D., et al. 2009, ApJL, 697, L137
Regev, O. 2006, Chaos and Complexity in Astrophysics (Cambridge Univ. Press)
Ribeiro, H. V., Zunino, L., Lenzi, E. K., Santoro, P. A., & Mendes, R. S. 2012, PLoSO, 7, e40689
Robertson, B. E., Tacchella, S., Johnson, B. D., et al. 2023, ApJL, 942, L42
Roli, A., Ligot, A., & Birattari, M. 2019, FrRAI, 6, 130
Rosso, O. A., Larrondo, H., Martin, M. T., Plastino, A., & Fuentes, M. A. 2007, PhRvL, 99, 154102
Segal, G., Parkinson, D., Norris, R. P., & Swan, J. 2019, PASP, 131, 108007
Shannon, C. E. 1948, The Bell System Technical Journal, 27, 379
Shore, S. N., & Galli, D. 2003, Ap&SS, 284, 809
Sigaki, H. Y., De Souza, R., De Souza, R., Zola, R., & Ribeiro, H. 2019, PhRvE, 99, 013311
Sigaki, H. Y., Perc, M., & Ribeiro, H. V. 2018, PNAS, 115, E8585
Singh, M. K., Chanu, A. L., Singh, R. B., & Singh, M. S. 2026, CSF, 207, 117971
Small, M., McCullough, M., & Sakellariou, K. 2018, in 2018 Int. Symp. on Circuits and Systems (ISCAS) (IEEE), 1
Soria, R., & Kong, A. K. H. 2002, ApJL, 572, L33
Thilker, D. A., Bianchi, L., Boissier, S., et al. 2005, ApJL, 619, L79
Thilker, D. A., Bianchi, L., Meurer, G., et al. 2007, ApJS, 173, 538
Vacca, W. D., Garmany, C. D., & Shull, J. M. 1996, ApJ, 460, 914
Watkins, E. J., Barnes, A. T., Henny, K., et al. 2023, ApJL, 944, L24
Weck, P. J., Schaffner, D. A., Brown, M. R., & Wicks, R. T. 2015, PhRvE, 91, 023101
Weygand, J. M., & Kivelson, M. G. 2019, ApJ, 872, 59
Williams, T. G., Sun, J., Barnes, A. T., et al. 2022, ApJL, 941, L27
Wolf, A., Swift, J. B., Swinney, H. L., & Vastano, J. A. 1985, PhyD, 16, 285
Yadav, J., Das, M., Patra, N. N., et al. 2021, ApJ, 914, 54
Yip, C. W., Connolly, A. J., Szalay, A. S., et al. 2004, AJ, 128, 585
Zaragoza-Cardiel, J., Fritz, J., Aretxaga, I., et al. 2019, MNRASL, 487, L61
Zhu, X.-P., Dai, J.-M., Bian, C.-J., et al. 2019, Ap&SS, 364, 55
Zunino, L., & Ribeiro, H. V. 2016, CSF, 91, 679